The Astrophysical Journal, 705:184–198, 2009 November 1 doi:10.1088/0004-637X/705/1/184

INFRARED LUMINOSITIES AND DUST PROPERTIES OF $z \approx 2$ DUST-OBSCURED GALAXIES

R. S. Bussmann[1], Arjun Dey[2], C. Borys[3], V. Desai[4], B. T. Jannuzi[2], E. Le Floc'h[5], J. Melbourne[6], K. Sheth[4], and B. T. Soifer[4,6]

[1] Steward Observatory, Department of Astronomy, University of Arizona, 933 N. Cherry Ave., Tucson, AZ 85721, USA; rsbussmann@as.arizona.edu
[2] National Optical Astronomy Observatory, 950 N. Cherry Ave., Tucson, AZ 85719, USA
[3] Herschel Science Center, California Institute of Technology, Pasadena, CA 91125, USA
[4] Spitzer Science Center, California Institute of Technology, MS 220-6, Pasadena, CA 91125, USA
[5] Spitzer Fellow, Institute for Astronomy, University of Hawaii, Honolulu, HI 96822, USA
[6] Division of Physics, Math and Astronomy, California Institute of Technology, Pasadena, CA 91125, USA

Received 2009 May 27; accepted 2009 September 16; published 2009 October 8

ABSTRACT

We present SHARC-II 350 μm imaging of twelve 24 μm bright ($F_{24\,\mu m} > 0.8$ mJy) Dust-Obscured Galaxies (DOGs) and Combined Array for Research in Millimeter-wave Astronomy (CARMA) 1 mm imaging of a subset of two DOGs. These objects are selected from the Boötes field of the NOAO Deep Wide-Field Survey. Detections of four DOGs at 350 μm imply infrared (IR) luminosities which are consistent to within a factor of 2 of expectations based on a warm-dust spectral energy distribution (SED) scaled to the observed 24 μm flux density. The 350 μm upper limits for the 8 non-detected DOGs are consistent with both Mrk 231 and M82 (warm-dust SEDs), but exclude cold dust (Arp 220) SEDs. The two DOGs targeted at 1 mm were not detected in our CARMA observations, placing strong constraints on the dust temperature: $T_{dust} > 35$–60 K. Assuming these dust properties apply to the entire sample, we find dust masses of $\approx 3 \times 10^8\ M_\odot$. In comparison to other dusty $z \sim 2$ galaxy populations such as submillimeter galaxies (SMGs) and other *Spitzer*-selected high-redshift sources, this sample of DOGs has higher IR luminosities ($2 \times 10^{13}\ L_\odot$ versus $6 \times 10^{12}\ L_\odot$ for the other galaxy populations) that are driven by warmer dust temperatures (>35–60 K versus ~30 K) and lower inferred dust masses ($3 \times 10^8\ M_\odot$ versus $3 \times 10^9\ M_\odot$). Wide-field *Herschel* and Submillimeter Common-User Bolometer Array-2 surveys should be able to detect hundreds of these power-law-dominated DOGs. We use the existing *Hubble Space Telescope* and *Spitzer*/InfraRed Array Camera data to estimate stellar masses of these sources and find that the stellar to gas mass ratio may be higher in our 24 μm bright sample of DOGs than in SMGs and other *Spitzer*-selected sources. Although much larger sample sizes are needed to provide a definitive conclusion, the data are consistent with an evolutionary trend in which the formation of massive galaxies at $z \sim 2$ involves a submillimeter bright, cold-dust, and star-formation-dominated phase followed by a 24 μm bright, warm-dust and AGN-dominated phase.

Key words: galaxies: evolution – galaxies: fundamental parameters – galaxies: high-redshift – submillimeter

Online-only material: color figures

1. INTRODUCTION

In the local universe, the most bolometrically luminous galaxies are dominated by thermal emission from dust which absorbs ultraviolet (UV) and optical light and re-radiates it in the infrared (IR; Soifer et al. 1986). While rare locally, these ultra-luminous IR galaxies (ULIRGs) are more common at high redshift (e.g., Franceschini et al. 2001; Le Floc'h et al. 2005; Pérez-González et al. 2005). Studies combining the improved sensitivity in the IR of the *Spitzer Space Telescope* with wide-field ground-based optical imaging have identified a subset of this $z \sim 2$ ULIRG population that is IR-bright but also optically faint (Yan et al. 2004; Houck et al. 2005; Weedman et al. 2006b; Fiore et al. 2008, 2009; Dey et al. 2008). In particular, Dey et al. (2008) and Fiore et al. (2008) present a simple and economical method for selecting these systems based on *R*-band and 24 μm Multiband Imaging Photometer for *Spitzer* (MIPS; Rieke et al. 2004) data. Dey et al. (2008) employ a color cut of $R-[24] > 14$ (Vega magnitudes; $\approx F_\nu(24\ \mu m)/F_\nu(R) > 1000$) to identify objects they call dust-obscured Galaxies (DOGs). Applied to the 8.6 deg^2 Boötes field of the NOAO Deep Wide-Field Survey (NDWFS) that has uniform MIPS 24 μm coverage for $F_\nu(24\ \mu m) > 0.3$ mJy, this selection yields a sample of ≈2600 DOGs, or ≈302 deg^{-2}.

The extreme red colors and number density of the DOGs imply that they are undergoing a very luminous, short-lived phase of activity characterized by vigorous stellar bulge and nuclear black hole growth. Spectroscopic redshifts determined for a subsample of DOGs using the Deep Imaging Multi-Object Spectrograph (DEIMOS; Faber et al. 2003) and the Low Resolution Imaging Spectrometer (LRIS; Oke et al. 1995) on the telescopes of the W. M. Keck Observatory (59 DOGs), as well as the Infrared Spectrometer (IRS; Houck et al. 2004) on *Spitzer* (47 DOGs) have revealed a redshift distribution centered on $z \approx 2$ with a dispersion of $\sigma_z \approx 0.5$ (Dey et al. 2008).

While DOGs are rare, they are sufficiently luminous (≈ 90% of DOGs with spectroscopic redshifts have $L_{IR} > 10^{12}\ L_\odot$) that they may contribute up to one-quarter of the total IR luminosity density from all $z \sim 2$ galaxies (and over half that from all ULIRGs at $z \sim 2$) and may be the progenitors of the most luminous ($\sim 4L^*$) present-day galaxies (Dey et al. 2008; Brodwin et al. 2008). Thus far, the efforts to estimate the IR luminosities of DOGs have primarily relied upon spectroscopic redshifts and the observed 24 μm flux density. Dey et al. (2008) use an empirical relation between the rest-frame 8 μm luminosity (computed from the observed 24 μm flux density) and the IR luminosity, derived by Caputi et al. (2007). However, there is evidence from sources with $F_{24\,\mu m} > 0.25$ mJy that

methods based on only the 24 μm flux density can overestimate the IR luminosity by factors of 2–10 (Papovich et al. 2007). Results from deep 70 μm and 160 μm imaging of a subsample of 24 μm bright DOGs are consistent with this, favoring hot-dust-dominated spectral energy distribution (SED) templates like that of Mrk 231 (Tyler et al. 2009) which lead to estimates of the IR luminosity that are on the low end of the range in $L_{\rm IR}/L_8$ conversion factors adopted in Dey et al. (2008).

In this paper, we present 350 μm and 1 mm photometry of a sample of DOGs whose mid-IR spectral features (silicate absorption, power-law SEDs) suggest the presence of a strong active galactic nucleus (AGN). The primary goals of this study are to measure their IR luminosities and constrain their dust properties, in particular the dust masses and temperatures. We also estimate stellar masses for the sources in the sample using published *Hubble Space Telescope* (*HST*) data and *Spitzer* InfraRed Array Camera (IRAC) catalogs from the *Spitzer* Deep Wide-Field Survey (SDWFS; see Ashby et al. 2009). Comparison of the stellar and dust masses potentially allows us to place constraints on the evolutionary status of these sources.

In Section 2, we present the details of the observations. Section 3 presents the DOG SEDs from 0.4 μm to 1 mm and IR luminosity measurements, constraints on the dust temperature, and dust and stellar mass estimates. In Section 4, we compare our results with similar studies of submillimeter galaxies (SMGs) and *Spitzer*-selected sources from the eXtragalactic First Look Survey (XFLS) and *Spitzer* Wide InfraRed Extragalactic (SWIRE) survey. We present our conclusions in Section 5.

Throughout this paper we assume a cosmology where $H_0 = 70$ km s^{-1} Mpc^{-1}, $\Omega_{\rm m} = 0.3$, and $\Omega_\lambda = 0.7$.

2. OBSERVATIONS

2.1. Sample Selection

Dey et al. (2008) identified 2603 DOGs in the 8.6 deg^2 NDWFS Boötes field, selecting all 24 μm sources satisfying $R - [24] > 14$ (Vega magnitude) and $F_{24\,\mu{\rm m}} > 0.3$ mJy. We identified 12 DOGs with spectroscopic redshifts for follow-up 350 μm imaging (see Figure 1) with the second-generation Submillimeter High Angular Resolution Camera (SHARC-II) at the Caltech Submillimeter Observatory (CSO). These targets were selected to have bright 24 μm flux densities ($F_{24\,\mu{\rm m}} \gtrsim 1$ mJy) and a power-law-dominated mid-IR SED (based on *Spitzer*/IRAC and 24 μm MIPS photometries; for details, see Section 3.1.2 in Dey et al. 2008). Using the deeper IRAC observations from SDWFS (Ashby et al. 2009), the fraction of DOGs qualifying as power-law sources ranges from ≈10% at $F_{24\,\mu{\rm m}} = 0.3$ mJy to ≈ 60% at $F_{24\,\mu{\rm m}} = 1$ mJy. As shown in Figure 1, our sample spans a broad range in the $R - [24]$ color (≈14.5–17.5). *Spitzer*/IRS spectroscopic redshifts have been obtained for these sources based on the 9.7 μm silicate absorption feature. Power-law continua and silicate absorption are typical features of AGN-dominated systems (Donley et al. 2007; Weedman et al. 2006a; Polletta et al. 2008; Brand et al. 2008). We note that such systems often exhibit intense star formation concurrent with the growth of a super-massive central black hole (e.g., Wang et al. 2008).

Details of our observations are presented in Table 1. The effective integration time (Column 8 of Table 1) represents the time necessary to reach the same noise level given a completely transparent atmosphere (see Coppin et al. 2008, for details).

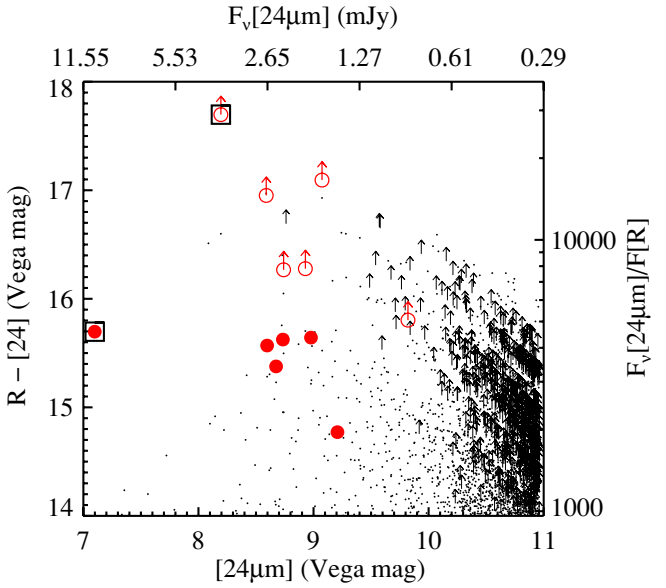

Figure 1. $R - [24]$ color vs. 24 μm mag for DOGs in the NDWFS Boötes field. Bottom and top abscissae show the 24 μm mag and flux density, respectively. Left and right ordinates show the color in magnitudes and the $F_{24\,\mu{\rm m}}/F_{0.7\,\mu{\rm m}}$ flux density ratio, respectively. Black dots and upward arrows show the full sample of DOGs, with and without an *R*-band detection, respectively. The subsample studied in this paper is represented by red circles (open symbols show sources undetected in the *R*-band data). Two sources observed by CARMA at 1 mm are highlighted by a black square. This plot demonstrates that the sample studied in this paper probes the 24 μm bright DOGs over a wide range of $R - [24]$ colors.
(A color version of this figure is available in the online journal.)

We observed two of the twelve DOGs at 1 mm using the Combined Array for Research in Millimeter-wave Astronomy (CARMA) interferometer to search for thermal emission from cold-dust particles. These were primarily selected to have robust 350 μm detections to enhance the probability of detection at 1 mm and, in the event of a non-detection, allow useful constraints to be placed on the dust properties. The two targets observed with CARMA are SST24 J142827.2+354127 (S2) and SST24 J143001.9+334538 (S3). Table 2 presents the date and integration time of the CARMA observations.

2.2. SHARC-II 350 μm Imaging and Photometry

The SHARC-II observations of the 12 target DOGs were carried out over the course of five separate observing runs from 2005 January to 2007 May. Data were collected only when the atmospheric opacity was low and conditions were stable ($\tau_{225\,\rm GHz} < 0.06$). Pointing, focus checks, and calibration were performed every hour, using ULIRG Arp 220 as a calibrator ($F_{350\,\mu{\rm m}} = 10.2 \pm 1.0$ Jy). Other secondary calibrators (CIT6, CRL2688, 3C345) were used occasionally to verify the Arp 220 calibrations. A non-connecting Lissajous pattern was used to modulate the telescope pointing with amplitudes of 15″–20″ and periods of 10–20 s. The observations made use of the CSO Dish Surface Optimization System to optimize the dish surface accuracy and beam efficiency (Leong et al. 2006).

Data were reduced using the Comprehensive Reduction Utility for SHARC-II (CRUSH) software package with the "deep" option to optimize the signal-to-noise ratio (S/N) for faint (< 100 mJy) point sources (Kovács 2006). The output map has a pixel scale of 1.″62 pixel^{-1}, and is smoothed with a 9″ Gaussian beam, resulting in an effective image FWHM of 12.″4.

A 20″ diameter aperture was used for photometry to compute the instrumental flux density of each source. The sky level and

Table 1
SHARC-II 350 μm Observations

Source Name	ID	R.A. (J2000)	Decl. (J2000)	z	UT Year-Month	$t_{\rm int}$[a] (hr)	$t_{\rm eff}$[b] (min)	$\sigma_{\rm map}$ (mJy)
SST24 J142648.9+332927	*S*1	14:26:48.970	+33:29:27.56	2.00[c]	2006-Apr	1.1	4.0	20
SST24 J142827.2+354127	*S*2	14:28:27.190	+35:41:27.71	1.293[d]	2005-Apr/2006-Apr/2007-May	3.3	11.9	10
SST24 J143001.9+334538	*S*3	14:30:01.910	+33:45:38.54	2.46[e]	2005-Apr/2006-Apr/2006-May	3.6	11.4	8
SST24 J143025.7+342957	*S*4	14:30:25.764	+34:29:57.29	2.545[f]	2006-Apr	1.0	2.0	26
SST24 J143135.2+325456	*S*5	14:31:35.309	+32:54:56.84	1.48[c]	2007-May	1.2	2.0	30
SST24 J143325.8+333736	*S*6	14:33:25.884	+33:37:36.90	1.90[c]	2006-Apr	0.3	1.2	28
SST24 J143411.0+331733	*S*7	14:34:10.980	+33:17:32.70	2.656[g]	2005-Jan	3.8	12.7	8
SST24 J143447.7+330230	*S*8	14:34:47.762	+33:02:30.46	1.78[e]	2007-May	1.8	10.5	10
SST24 J143508.4+334739	*S*9	14:35:08.518	+33:47:39.44	2.10[c]	2006-Apr	1.0	0.5	35
SST24 J143539.3+334159	*S*10	14:35:39.364	+33:41:59.13	2.62[e]	2005-Apr/2006-Apr	2.5	3.1	15
SST24 J143545.1+342831	*S*11	14:35:45.137	+34:28:31.42	2.50[c]	2006-Apr	0.8	3.2	22
SST24 J143644.2+350627	*S*12	14:36:44.269	+35:06:27.12	1.95[e]	2006-Apr/2006-May	2.1	6.7	10

Notes.
[a] Actual on-source integration time.
[b] Effective integration time for a transparent atmosphere (Coppin et al. 2008).
[c] Redshift from *Spitzer*/IRS (S. Higdon et al. 2010, in preparation).
[d] Redshift from Keck DEIMOS (Desai et al. 2006).
[e] Redshift from *Spitzer*/IRS (Houck et al. 2005).
[f] Redshift from Keck DEIMOS (A. Dey et al. 2010, in preparation).
[g] Redshift from Keck LRIS (Dey et al. 2005).

Table 2
CARMA 1 mm Observations

ID	UT Year-Month	$t_{\rm int}$ (hr)[a]
S2	2008-Apr/May	10.3
S3	2008-Apr/May	7.5

Note. [a] On-source integration time.

photometric uncertainty were computed by measuring the mean and rms in ≈10 off-source 20″ diameter apertures. The same procedure was applied to the calibration images, and a scaling factor was derived that converts the instrumental flux density to a physical flux density (using this method, no subsequent aperture correction is required as long as both the science and calibration targets are unresolved and measured in the same aperture).

The aperture photometry is consistent with peak flux density measurements in all but one source, SST24 J142648.9+332927. This source has a radial profile that is significantly more extended than the point-spread function of the final map, which results in the peak flux underestimating the aperture flux density measurement. The extended structure in the image is more likely to be noise than signal, so in this case we report the peak flux measurement, which is formally a non-detection.

Flux boosting of low-S/N sources can be an important effect in wide-field surveys where source positions are not known a priori (e.g., Coppin et al. 2005). However, because we know our source positions at the $< 1''$ level (from MIPS and IRAC centroids), flux boosting is not a significant effect, and so we do not apply any such corrections to our measurements. Our approach follows that adopted by Laurent et al. (2006) and Kovács et al. (2006) in their 350 μm follow-up imaging of SMGs.

2.3. CARMA 1 mm Imaging and Photometry

The CARMA observations were obtained between 2008 April 7 and May 1 in the C-array configuration (beamsize is $\approx 2 \times 1$ arcsec^2). A total of 7.5 hr and 10.3 hr of integration time in good 1 mm weather conditions were spent on sources SST24 J143001.9+334538 (S3) and SST24 J142827.2+354127 (S2), respectively. These sources were selected primarily because of their robust (S/N > 4.5) detections at 350 μm. In addition, source S3 is detected with *Spitzer*/MIPS at 70 μm and 160 μm (Tyler et al. 2009), while S2 is the subject of a detailed spectroscopic study (Desai et al. 2006).

System temperatures were in the range 250–400 K. A correlator configuration was used with three adjacent 15 × 31 MHz bands centered on 220 GHz, the frequency at which the CARMA 1 mm receivers are most sensitive. The quasar J1310+323 (chosen for its spatial proximity) was observed every 15 minutes for amplitude and phase calibration. Quasars 3C 273 and MWC 349 were used for pointing, passband calibration, and flux calibration.

Data were reduced using the Multichannel Image Reconstruction, Image Analysis, and Display (MIRIAD) software package (Sault et al. 1995). Visual inspection of visibilities as a function of baseline length allowed us to identify and flag spurious data. A cleaned map was generated for each track of integration time (ranging from 1 to 5 hr in length) and these tracks were co-added together using a weighted mean to obtain a final image of these sources. No detections were found in either case. Both sources are unresolved in the IRAC images, and NICMOS/F160W imaging of S3 indicates a size of $\lesssim 0\farcs5$, implying that it is very unlikely any emission was resolved out by the interferometer. The IMSTAT routine from MIRIAD was used to determine the noise level in the co-added images where we expected to see the source. Table 3 shows the photometry from 24 μm to 1 mm, where available. Non-detections are given as 3σ upper limits.

2.4. Optical, Near-IR, Mid-IR, and Far-IR Photometry

The optical and near-IR photometries used in this paper to estimate stellar masses are based on high spatial-resolution *HST* data (WFPC2/F606W, ACS/F814W, and NIC2/F160W) published in Bussmann et al. (2009). The *HST* data allow

Table 3
Photometry[a]

Source Name	$R-[24]$ (Vega magnitude)	$F_{24\,\mu m}$ (mJy)	$F_{70\,\mu m}$ (mJy)	$F_{160\,\mu m}$ (mJy)	$F_{350\,\mu m}$ (mJy)	$F_{1.2\,mm}$ (mJy)	$F_{20\,cm}$[b] (mJy)
S1	> 16.1	2.33 ± 0.07	···	···	< 66	···	···
S2	15.7	10.55 ± 0.13	···	<45[c]	74 ± 13	<1.5	···
S3	> 17.4	3.84 ± 0.06	9.3 ± 2.3[d]	65 ± 11[d]	41 ± 13	<1.8	0.42 ± 0.04
S4	15.1	2.47 ± 0.05	···	···	<81	···	0.23 ± 0.03
S5	14.5	1.51 ± 0.05	···	···	<100	···	0.54 ± 0.12
S6	15.4	1.87 ± 0.06	···	···	<137	···	0.20 ± 0.03
S7	12.4[e]	0.86 ± 0.05	<25[f]	<90[f]	37 ± 13	···	···
S8	> 16.8	1.71 ± 0.04	···	···	45 ± 12	···	0.31 ± 0.06
S9	15.3	2.65 ± 0.08	···	···	<150	···	0.24 ± 0.04
S10	> 16.7	2.67 ± 0.06	<8.1[d]	<38[d]	<50	···	···
S11	>16.0	1.95 ± 0.05	···	···	<60	···	···
S12	15.4	2.34 ± 0.05	9.1 ± 2.5	43 ± 12	<34	···	5.1 ± 0.2

Notes.
[a] Upper limits quoted are 3σ values.
[b] Photometry from Westerbork Synthesis Radio Telescope imaging de Vries et al. (2002).
[c] Photometry from Desai et al. (2006).
[d] Photometry from Tyler et al. (2009).
[e] *R*-band photometry includes diffuse emission from Ly-α nebula (Dey et al. 2005).
[f] Photometry from Dey et al. (2005).

the separation of an unresolved nuclear component (flux on scales $\lesssim$ 1 kpc) from a more spatially extended component. Because the AGN contribution in the rest-frame UV to optical is uncertain, the photometry of the extended component is used here (measured with 2″ diameter apertures) to ensure that our stellar mass estimates are not biased by the presence of an obscured AGN (for details on how the extended component is computed, see Bussmann et al. 2009). Additionally, 4″ diameter aperture photometry in the optical (B_W, R, and I) from the NDWFS is shown in the SEDs of the objects in this sample (details on how the photometry is computed may be found in Bussmann et al. 2009).

The mid-IR photometries used in this paper are from the publicly available Data Release 1.1 (DR1.1) catalogs from the SDWFS IRAC coverage of the Boötes field (Ashby et al. 2009). The SDWFS catalogs incorporate the earlier IRAC Shallow Survey of the Boötes field undertaken by the IRAC guaranteed time observation (GTO) programs (Eisenhardt et al. 2004). We identified IRAC counterparts of the DOGs in this paper from the SDWFS catalogs using a 3″ search radius centered on the 24 μm position (the MIPS 24 μm 1σ positional uncertainty is 1.″2). All of the DOGs in this paper have IRAC counterparts, detected at $> 4\sigma$ in all four IRAC channels. We use the 4″ (rather than the 6″) diameter aperture photometry from the DR1.1 SDWFS catalog to reduce contamination from nearby sources. We note that aperture corrections derived from isolated, bright stars have been applied to the SDWFS catalogs.

Finally, 24, 70, and 160 μm data over 8.61 deg^2 of the Boötes field are available from GTO programs. The data were reduced by the MIPS GTO team and reach 1σ rms depths of 51 μJy, 5 mJy, and 18 mJy at 24, 70, and 160 μm, respectively. Details of the GTO surveys, such as mapping strategy, data reduction, and source catalogs, will be discussed elsewhere. In addition, several of the DOGs in this paper were targeted for deeper MIPS photometric observations by *Spitzer* General Observer program 20303 (P.I. E. LeFloc'h), and the results are reported in Tyler et al. (2009). We use the Tyler et al. (2009) measurements where they are available.

3. RESULTS

In this section, we present SEDs from 0.4 μm to 1 mm for each source in our sample and compare with local starburst (M82) and ULIRG (Arp 220 and Mrk 231) templates. Our approach is to artificially redshift the local galaxy templates and normalize them to match the DOG photometry at observed-frame 24 μm. This allows a simple, qualitative comparison of DOGs and galaxies with properties ranging from warm-dust, star-formation-dominated (M82), to cool dust, star-formation-dominated (Arp 220), to warm-dust, AGN-dominated (Mrk 231). We will use the SED that provides the best fit over the sampled wavelength range (observed optical through submillimeter) to estimate the IR luminosities of the DOGs.

Later in this section, we use our limits at 1 mm from CARMA to place constraints on the dust temperatures and limits on the dust masses of DOGs. Finally, we use *HST* and *Spitzer*/IRAC data to estimate stellar masses of DOGs.

3.1. Qualitative SED Comparison

Figures 2 and 3 show the SEDs of the sources, divided respectively into those with and those without detections at 350 μm. Note that the rest-frame UV photometry for source S7 is contaminated by emission from nearby sources and will be treated in more detail in a future paper (M. Prescott et al. 2010, in preparation).

Overplotted in each panel are M82 (Silva et al. 1998),[7] Mrk 231 (R.-R. Chary 2008, private communication), and Arp 220 (Rieke et al. 2009) templates, placed at the appropriate redshift and scaled to match the flux density observed in the MIPS 24 μm band. The scaling factors derived for the three templates range over 200–900, and 2–10, 70–700, respectively (the deep silicate absorption feature in Arp 220 and the strong polycyclic aromatic hydrocarbon (PAH) emission feature of M82 make the scaling factors closer to each other than a simple estimate based on the ratio of the IR luminosities would imply).

[7] We use a slightly updated SED obtained from http://adlibitum.oat.ts.astro.it/silva/grasil/modlib/modlib.html

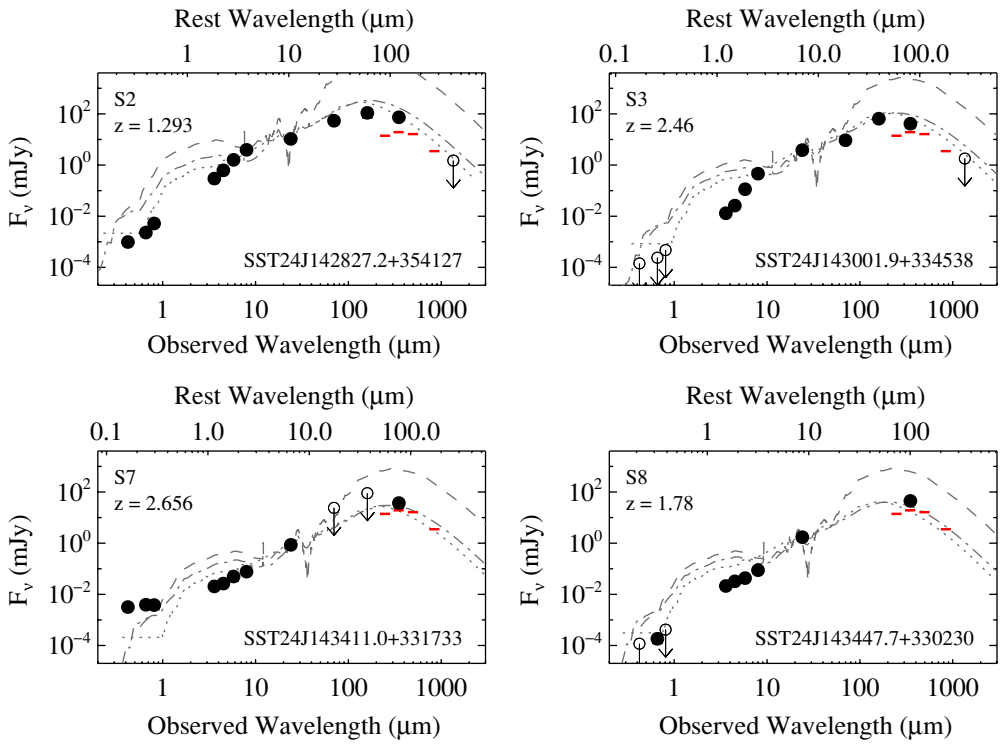

Figure 2. SEDs of five DOGs detected by SHARC-II at 350 μm. Dotted, dashed, and dot-dashed lines show the Mrk 231, Arp 220, and M82 template SEDs, respectively, placed at the appropriate redshift and scaled to match the observed 24 μm flux density. Red horizontal lines show the 5σ sensitivity limits (ignoring confusion) from the planned wide-field *Herschel* surveys at 250, 350, and 500 μm, and SCUBA-2 surveys at 850 μm. The cool dust SED of Arp 220 significantly overpredicts the 350 μm flux density in all cases. The warm dust SED of M82 provides a better fit in the far-IR, but Mrk 231 provides the best fit in both the far-IR and the optical.

(A color version of this figure is available in the online journal.)

For the Arp 220 and Mrk 231 templates, we have interpolated the spectrum in the UV to match Galaxy Evolution Explorer photometry (in the case of Arp 220) and International Ultraviolet Explorer data as well as *HST* Faint Object Spectrograph data (in the case of Mrk 231; Hutchings & Neff 1987; Gallagher et al. 2002).

These templates were chosen because they sample a range of dust temperatures and AGN/starburst contributions. M82 is one of the closest (d_L = 3.86 Mpc) galaxies undergoing a starburst, as it was triggered by a recent interaction with M81. Although it is less luminous than DOGs ($L_{\rm IR} \approx 6 \times 10^{10}\ L_\odot$;[8] Sanders et al. 2003), its nucleus is dominated by a warm-dust component ($T_{\rm dust}$ = 48 K; Hughes et al. 1994). Arp 220 is a nearby (d_L = 77.3 Mpc) ULIRG ($L_{\rm IR} \approx 1.6 \times 10^{12}\ L_\odot$; Sanders et al. 2003) dominated by cold dust ($T_{\rm dust}$ = 35 K; Rigopoulou et al. 1996). Mrk 231 is another nearby (d_L = 175.1 Mpc) ULIRG ($L_{\rm IR} \approx 3.2 \times 10^{12}\ L_\odot$; Sanders et al. 2003), but has a warm dust ($T_{\rm dust}$ = 51 K; Yang & Phillips 2007) SED dominated by an obscured AGN.

Qualitatively, the Mrk 231 template provides a much better fit than the Arp 220 template to the 350 μm photometry in every case. M82 fits the 24 μm and 350 μm photometries reasonably well (although not as well as Mrk 231), but it fares poorly in the mid-IR and optical, where a strong stellar component in M82 is not seen in the DOGs in this sample (which are dominated by a power law in the mid-IR). Additionally, M82 shows strong PAH emission which is not seen in the power-law DOGs.

The red horizontal bars in Figures 2 and 3 show 5σ limits (ignoring confusion) from planned wide-field (> 8 deg^2) surveys with the *Herschel* Space Observatory (shown for the channels at 250, 350, and 500 μm) and with the Submillimeter Common-User Bolometer Array-2 (SCUBA-2) instrument at 850 μm. Most of the power-law DOGs studied in this paper have SEDs that peak around observed frame 250 μm, which is where the *Herschel* wide-field maps will be the deepest (5σ limit of 14 mJy). If all of the 24 μm bright DOGs are detected at 250 μm in the two wide-field surveys that are planned to reach the depths assumed here (Lockman Hole east, 11 deg^2; Extended *Chandra* Deep Field South, 8 deg^2), then a total of ≈600 power-law DOGs should be detected in the 250 μm *Herschel* catalogs of these two fields. The SCUBA-2 surveys of these fields should be deep enough (5σ limit of 3.5 mJy at 850 μm) to detect many of these sources, allowing dust temperature constraints to be placed on a statistically significant sample of these rare, important objects.

Figure 4 shows all of the DOG SEDs on the same plot, normalized by the rest-frame 8 μm flux density (which is estimated from the observed-frame 24 μm flux density by assuming a power law of the form $F_\nu \propto \nu^\alpha$, where $\alpha = -2$). The SEDs M82, Arp 220, Mrk 231, and a composite SMG template SED spanning mid-IR to submillimeter wavelengths are also shown. The composite SMG template is derived from bright ($F_{850\,\mu{\rm m}} > 5$ mJy) SMGs from the Great Observatories Origins Deep Survey North (GOODS-N) field with mid-IR spectra (Pope et al. 2008b).

One striking feature of this plot is the steep slope shown by DOGs in the rest-frame 1–4 μm. Whereas Mrk 231, M82, and Arp 220 all exhibit a bump in the 1–2 μm regime, no such feature is apparent in the DOG SEDs. This could be due to the presence of an obscured AGN outshining the stellar light,

[8] $L_{\rm IR}$ is the luminosity integrated over 8–1000 μm.

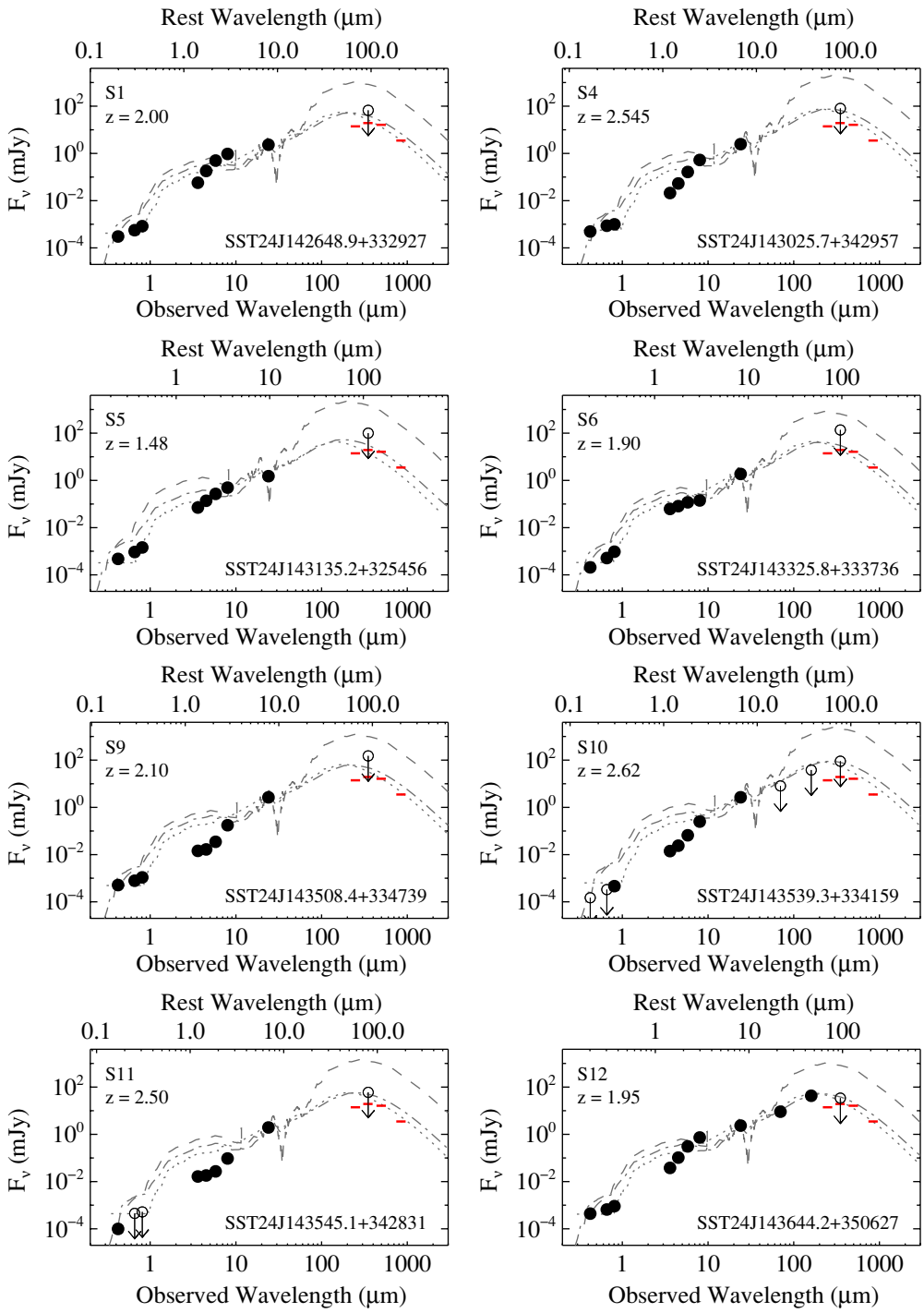

Figure 3. Same as Figure 2, except showing SEDs of seven DOGs not detected by SHARC-II at 350 μm. The limits at 350 μm are all inconsistent with the Arp 220 SED. The 250 μm channel of *Herschel* should be very efficient for detecting power-law DOGs in wide-field surveys, assuming that Mrk 231 is an appropriate representation of the far-IR SED.

(A color version of this figure is available in the online journal.)

in the rest-frame near-IR. This is in contrast to rest-frame UV and optical wavelengths, where *HST* imaging has revealed that stellar light appears to dominate (Bussmann et al. 2009). As noted previously, DOGs have far-IR to mid-IR flux density ratios more similar to Mrk 231 than Arp 220. The composite SMG template overpredicts the far-IR flux for a given mid-IR flux in all cases where we have 350 μm detections. We note that adding an additional warm-dust component ($T_{\rm dust} = 350$ K; possibly powered by an AGN) to the composite SMG SED (as was done in Pope et al. 2008a) improves the quality of the fit over the rest-frame 8–100 μm. However, this composite SMG + AGN template retains a strong cool dust ($T_{\rm dust} \approx 30$ K) component that overpredicts the amount of emission at 1 mm. If this type of SED was appropriate for the power-law DOGs investigated in this paper, they would have been easily detected by CARMA.

An alternative way of displaying this information is shown in Figure 5. In each panel, the flux density ratio far-IR:mid-IR is plotted as a function of the flux density ratio mid-IR:optical

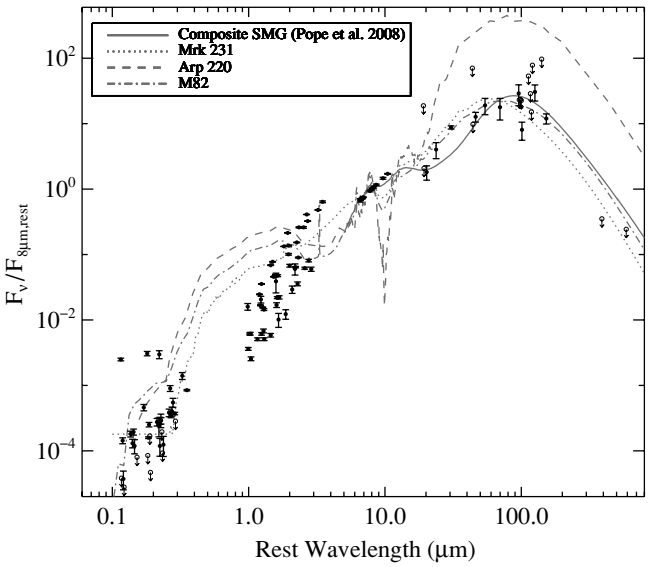

Figure 4. Optical through submillimeter SEDs of DOGs in the SHARC-II sample. Flux densities have been normalized by the rest-frame 8 μm flux density, computed from the observed 24 μm flux density. Of the three local galaxy templates shown, Mrk 231 provides the best fit over the rest-frame UV through submillimeter range because it has a warm dust SED (unlike Arp 220) and because it lacks a strong stellar component (unlike both Arp 220 and M82). None of the template SEDs match the steepness of the rest-frame near-IR photometry of the power-law DOGs. This may indicate that obscured AGNs dominate stellar emission to a greater extent in power-law DOGs than in Mrk 231.

($F_{24\,\mu m}/F_{0.7\,\mu m}$). The top two panels show $F_{350\,\mu m}/F_{24\,\mu m}$ on the y-axis, while the bottom two panels show $F_{1200\,\mu m}/F_{24\,\mu m}$ on the y-axis. SMGs and various *Spitzer*-selected sources are shown in the plots, divided into those that are detected in the (sub-)millimeter on the left and those that are not detected on the right. The SMG, XFLS, and SWIRE R-band data come from Dye et al. (2008), Yan et al. (2007), and Lonsdale et al. (2009), respectively. For SMGs without detections at 1200 μm, $F_{1200\,\mu m}$ is estimated using the 850 μm flux density and the dust temperature from Coppin et al. (2008), and is represented by a red cross symbol. Dotted, dashed, and dot-dashed lines indicate the evolution of Mrk 231, Arp 220, and M82, respectively, on this diagram over redshifts of 1–3. Compared to SMGs, DOGs in this sample have redder flux density ratios in the mid-IR:optical but bluer far-IR:mid-IR ratios. This cannot be explained by an enhancement of the 24 μm flux due to PAH emission, since mid-IR spectra of these DOGs show power-law continua with silicate absorption and weak or absent PAH emission features (Houck et al. 2005). Instead, the most likely explanation is that obscured AGN emission boosts the mid-IR continuum (e.g., Rieke & Lebofsky 1981) relative to both the optical and far-IR.

3.2. IR Luminosities

In this section, we provide the best available estimates of the total IR luminosities (L_{IR}; 8–1000 μm rest-frame) of the sample in this paper based on the 350 μm imaging. We then compare these with estimates based solely on the 24 μm flux density, and also with estimates of the far-IR luminosity (L_{FIR}; 40–500 μm, rest-frame) based on a modified black body which has been scaled to match the submillimeter photometry.

The qualitative SED comparison from Section 3.1 suggests that Mrk 231 provides a reasonable fit to the far-IR photometry. In addition, analysis of the 70 μm and 160 μm photometry of a sample of these types of AGN-dominated DOGs has suggested

Table 4
Luminosities

Source Name	L_{IR}[a] (10^{12} $L_\odot$)	$\nu L_\nu(8\,\mu m)$ (10^{12} $L_\odot$)	L_{IR}[b] (10^{12} $L_\odot$)	L_{FIR}[d] (10^{12} $L_\odot$)
S1	< 32[e]	2.2	23	...
S2	26 ± 5[d]	2.4	25	9.1
S3	22 ± 7[d]	7.2	81	10
S4	< 44[e]	5.2	57	...
S5	< 40[e]	53	5.1	...
S6	< 64[e]	1.5	15	...
S7	21 ± 7[d]	2.1	22	...
S8	20 ± 5[d]	1.1	11	...
S9	< 75[e]	2.9	31	...
S10	< 28[e]	6.2	69	...
S11	< 33[e]	3.9	42	...
S12	< 16[e]	2.0	21	...

Notes.
[a] Integral over 8–1000 μm of redshifted Mrk 231 template normalized at 350 μm.
[b] Estimated from νL_ν (8 μm)–L_{IR} relation from Caputi et al. (2007).
[c] Integral over 40–500 μm of best-fit-modified blackbody (only sources with CARMA 1 mm data).
[d] Uncertainties shown reflect 350 μm photometric uncertainties. Additional systematic uncertainties associated with the adoption of a Mrk 231 template are not included.
[e] 3σ upper limits.

that Mrk 231 provides a reasonable approximation of the full SED (Tyler et al. 2009, see Table 3 for overlap between that study and this one). Therefore, as the best measure of L_{IR}, we integrate (over 8–1000 μm rest-frame) a redshifted Mrk 231 template which has been scaled to match the observed 350 μm flux density (or 3σ limit, in the case of a non-detection). These values are tabulated in the first column of Table 4. For sources with detections at 350 μm, L_{IR} is in the range of $(2.0–2.6) \times 10^{13}$ $L_\odot$, with a median value of 2.2×10^{13} $L_\odot$.

The second column of Table 4 shows the rest-frame 8 μm luminosity, $\nu L_\nu(8\,\mu m)$, while the third column shows the total IR luminosity (8–1000 μm, rest frame) based on the spectroscopic redshift and an empirically determined relationship between $\nu L_\nu(8\,\mu m)$ and L_{IR}: $L_{IR} = 1.91 L_8^{1.06}$ (Caputi et al. 2007). This approach was used by Dey et al. (2008) in determining the contribution of DOGs to the total IR luminosity density of all $z \sim 2$ galaxies. L_{IR} values range over $(0.5–8.1) \times 10^{13}$ $L_\odot$, with a median value of 2.3×10^{13} $L_\odot$. The Caputi et al. derived value for L_{IR} is consistent with the 350 μm based estimate (or 3σ limit, in the case of non-detections) in 6/12 of the power-law DOGs studied here. In the remaining half of the sample, the Caputi et al. relation overestimates L_{IR} in 5/6 targets. In only one DOG (S8) is the 350 μm emission brighter than would be expected based on the 24 μm flux density, redshift, and the Caputi et al. relation. This implies that measurements of the IR luminosity density of DOGs relying solely on the 24 μm flux density will tend to overestimate their true contribution, consistent with what has been found in a recent study of faint ($F_{24\,\mu m} \sim$ 100–500 μJy) DOGs in GOODS-N (Pope et al. 2008a). Quantifying the extent of this effect will require much larger samples of DOGs with submillimeter measurements, the kind that will result from wide-field surveys with *Herschel* and SCUBA-2.

Finally, the last column of Table 4 shows FIR luminosities computed from the integral over 40–500 μm (rest frame) of the best-fit-modified blackbody (described in more detail in Section 3.3). These values are tabulated only for those sources with CARMA 1 mm imaging. We find L_{FIR} values of $\approx 10^{13}$ $L_\odot$,

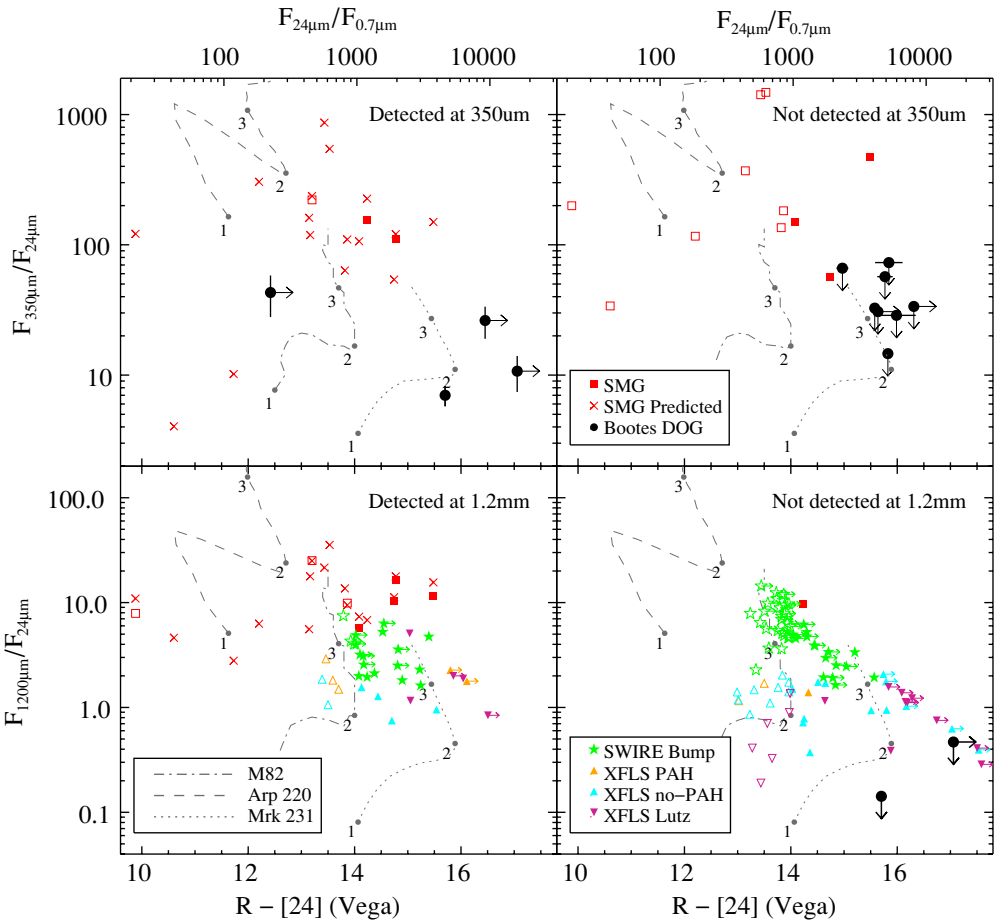

Figure 5. Top and bottom panels show 350 μm/24 μm and 1200 μm/24 μm flux density ratios, respectively, as a function of $R - [24]$ (Vega magnitude) color. For clarity, sources are separated into those detected at 350 μm or 1200 μm on the left and those that are not detected on the right. Objects that qualify as a DOG (R - [24] > 14) are shown with a filled symbol. Black circles indicate DOGs in Boötes. Red squares show measurements of SMGs (Coppin et al. 2008), while red crosses show predicted values based on the 850 μm photometry (see the text for details). Green stars show *Spitzer*-selected bump sources from SWIRE (Lonsdale et al. 2009). Orange triangles (teal triangles) show similarly identified sources from the XFLS dominated by PAH emission (silicate absorption) features (Sajina et al. 2008). Magenta inverted triangles show XFLS sources from Sajina et al. (2008). Finally, dotted, dashed, and dot-dashed lines show the evolution of Mrk 231, Arp 220, and M82 in this parameter space over redshifts 1–3. The DOGs studied in this paper have some of the reddest $R - [24]$ colors and lowest far-IR/mid-IR flux density ratios of other $z \sim 2$ ULIRGs like SMGs or other *Spitzer*-selected sources.

(A color version of this figure is available in the online journal.)

implying $L_{\rm IR}/L_{\rm FIR} \approx 3$. In contrast, Mrk 231 has $L_{\rm IR}/L_{\rm FIR} \approx 2$, underscoring the fact that the IR luminosity of these DOGs is dominated by mid-IR emission rather than FIR emission.

3.3. Constraints on Dust Properties

Additional constraints can be placed on the nature of the cold-dust emission from the two sources (S2 and S3) with CARMA. The 1 mm non-detections imply warm-dust temperatures. If we compute the predicted flux density at 1 mm based on the observed 24 μm flux density and assuming the three local galaxy SED templates (M82, Arp 220, and Mrk 231) used in the previous sections, we find values of 4.4, 740, 1.8 mJy, and 5.8, 120, 2.7 mJy for the two sources respectively. For S2, this implies that our 3σ limit (< 1.5 mJy) is close to the level we would expect if Mrk 231 is an appropriate SED, while the other two SEDs are clearly inconsistent with the data. For S3, the limit (< 1.8 mJy) is inconsistent with each of the SEDs, implying a warmer dust temperature than even Mrk 231.

A more quantitative approach is to minimize the residuals between the 160 μm, 350 μm, and 1 mm data and that expected from a modified blackbody. Doing this, we can constrain the dust temperature, $T_{\rm dust}$, and the dust emissivity index, β, of each target. The best-fit quantities and their uncertainties are estimated using a bootstrap technique that mimics the procedure used by Dunne et al. (2000). Briefly, for each flux density measurement, a set of 100 artificial flux densities is generated using a Gaussian random number generator. The mean value and dispersion of the distribution of artificial flux densities are set by the measurement value and its 1σ uncertainty, respectively (for non-detections, we assume a mean value of 0 and force artificial flux densities to be positive). Each artificial SED is used to construct a distribution of best-fit scaling factors and associated χ^2_ν values for a modified blackbody with a given combination of β and $T_{\rm dust}$.

Figure 6 shows the median χ^2_ν contours for the grid of $T_{\rm dust}$ and β values we have sampled in the model fitting for each source observed by CARMA. The contours show the degeneracy between β and $T_{\rm dust}$, and illustrate why a perfect fit is not possible in spite of the fact that a model with three parameters is being fitted to three data points (i.e., the input parameters are not fully independent). The distribution of $T_{\rm dust}$ found for SMGs based on 350 μm imaging from Coppin et al. (2008) and Kovács et al. (2006) is displayed in the lower panel. Two-sided Kolmogorov–Smirnov tests suggest that the distribution of $T_{\rm dust}$ (assuming $\beta = 1.5$) for each CARMA target is highly unlikely to be drawn from the same parent distribution as the combined

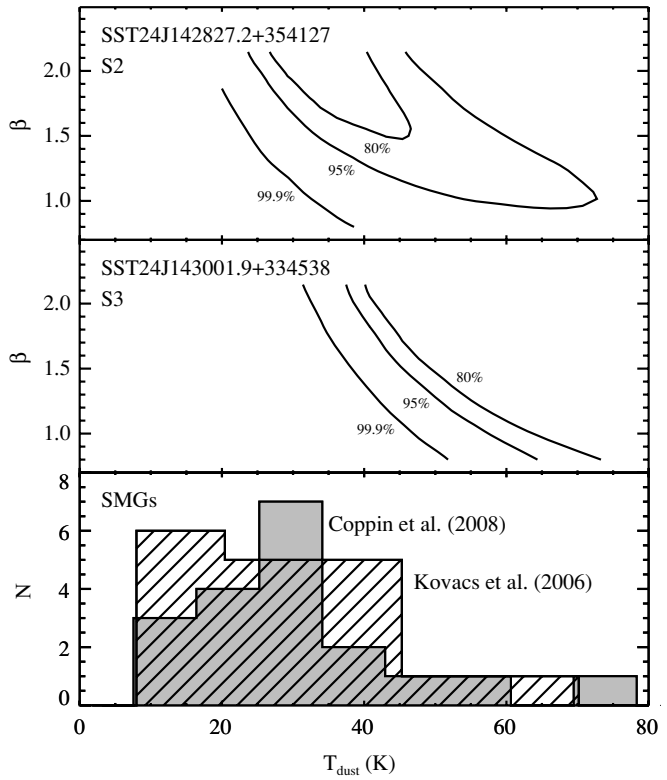

Figure 6. χ^2_ν contours based on modified blackbody fits to sources with CARMA data. Lines indicate 80%, 95%, and 99.9% confidence intervals. Also shown are $T_{\rm dust}$ distributions for SMGs with 350 μm data (Kovács et al. 2006; Coppin et al. 2008). The 95% confidence levels for S2 and S3 suggest dust temperature limits that would place them in the warmest 50% and 15%, respectively, of SMGs.

sample of SMGs (4% and 0.008%, for the two CARMA targets, respectively). In both of the CARMA targets, warmer dust temperatures are required due to the non-detection at 1 mm. The data cannot rule out models with higher values of β, but models of dust grains as well as Galactic and extra-galactic observations consistently suggest $\beta = 1$–2 (Hildebrand 1983; Dunne & Eales 2001). For $\beta = 1.5$, we reject $T_{\rm dust} \leqslant 33$ K and 45 K at the 95% confidence level, in S2 and S3 respectively. For $\beta = 2$, we can reject $T_{\rm dust} \leqslant 25$ K and 37 K.

It is also worth comparing our results with a similar set of 12 $z \sim 2$ ULIRGs selected on the basis of their observed mid-IR colors ($0.0 < [3.6] - [4.5] < 0.4$ and $0.7 < [3.6] - [8.0] < 0.5$) to lie at high redshift ($1.5 < z < 3$) (Younger et al. 2009). On the basis of 160 μm and 1.2 mm photometries, these authors find a range of dust temperatures of 35–45 K. This is slightly cooler than the lower limits we find in our sample of DOGs yet slightly warmer than the median of the SMG $T_{\rm dust}$ distribution.

Finally, another population of $z \sim 2$ ULIRGs exists that may be complementary to the DOGs studied here. These are objects selected to be radio-bright and submillimeter faint, and recently found to have bright 70 μm flux densities that imply they are warm-dust, starburst-dominated systems (Casey et al. 2009). Detailed comparisons of the mid-IR and far-IR properties of these populations will be valuable.

3.4. Dust Masses

Assuming optically thin submillimeter emission, cold-dust masses can be estimated from the 350 μm photometry (Hughes et al. 1997):

$$M_{\rm dust} = \frac{1}{1+z}\frac{S_{\rm obs} D_L^2}{\kappa_d^{\rm rest} B(\nu^{\rm rest},\ T_{\rm dust})}, \quad (1)$$

where $S_{\rm obs}$ is the observed 350 μm flux density, and $\kappa_d^{\rm rest}$ and $B(\nu^{\rm rest}, T_{\rm dust})$ are, respectively, the values of the mass absorption coefficient and blackbody function at the rest frequency $\nu^{\rm rest}$ and dust temperature $T_{\rm dust}$. The appropriate value for κ_d is uncertain to at least a factor of 2 (Dunne et al. 2003); we use a $\kappa_d^{\rm rest}$ value interpolated from Draine (2003) ($\langle\kappa_d^{\rm rest}\rangle \approx 20$ cm^2 g^{-1}).

The results from Section 3.3 suggest that $T_{\rm dust} > 35$–60 K for two of the sources. Adopting the average of these limits ($T_{\rm dust} = 45$ K) for all of the sources in this sample, dust mass limits are in the range (4.1–7.9) $\times 10^8$ $M_\odot$ (median value of 5.1×10^8 $M_\odot$) for the five objects with detections at 350 μm. The 3σ upper limits on the dust masses of the remaining sample range from (3–15) $\times 10^8$ $M_\odot$. Warmer values of $T_{\rm dust}$ would lead to smaller inferred dust masses (e.g., increasing the dust temperature by 10 K implies ≈50% lower dust masses). The dust masses are presented in Table 5.

These values agree with those of Bussmann et al. (2009), where dust masses of a sample of 31 power-law-dominated DOGs were estimated using predicted 850 μm flux densities based on Mrk 231 templates and the measured 24 μm flux density. In previous work, we assumed a $T_{\rm dust}$ of 75 K and found a median dust mass of 1.6×10^8 $M_\odot$. This is consistent with the notion that Mrk 231 accurately characterizes the far-IR SED of power-law DOGs, as described in Section 3.1 and in Tyler et al. (2009).

Finally, assuming a gas mass to dust mass ratio of 120 (as was found in a study of the nuclear regions of nearby LIRGs; see Wilson et al. 2008), the gas masses can be estimated as well. Using the assumed ratio, we find gas masses of (5–10) $\times$ 10^{10} $M_\odot$ (median value of 6×10^{10} $M_\odot$) for the detected objects and gas mass 3σ limits of (4–18) $\times 10^{10}$ $M_\odot$ in the remaining sample. We caution that this is very uncertain; Kovács et al. (2006) report a gas mass to dust mass ratio of ≈ 60 for SMGs, assuming $\kappa_d^{\rm rest} = 15$ cm^2 g^{-1}. If this gas to dust mass ratio is appropriate for our sample, then the implied gas masses will be a factor of 2 lower (2–5 $\times 10^{10}$ $M_\odot$).

Table 5
Dust Masses and Stellar Properties

Source Name	$M_{\rm dust}$[a] (10^8 $M_\odot$)	$M_{\rm star}$[b] (10^{10} $M_\odot$)	$M_{\rm star}/M_{\rm gas}$
S1	< 6.3	(0.3–1.5)	0.05–0.24
S2	7.9 ± 1.4	...	...
S3	4.9 ± 1.5	< 10	< 1.7
S4	< 5.5	(1–3)	> 0.15–0.45
S5	< 6.2	(1.5–3)	> 0.20–0.40
S6	< 7.5	(10–20)	> 1.1–2.2
S7	2.7 ± 0.7	...	...
S8	2.5 ± 0.9	> 1	> 0.33
S9	< 8.5	(0.6–1.1)	> 0.06–0.11
S10	< 6.5	(0.5–3)	> 0.06–0.38
S11	< 4.0	(> 10)	> 2.1
S12	< 1.9	(1–2)	> 0.44–0.88

Notes.
[a] Dust mass assuming $T_{\rm dust} = 45$ K.
[b] Stellar mass estimated from fitting photometry in the rest-frame UV and optical (V/I and H, respectively). Range given reflects 95% confidence intervals based only on photometric uncertainty.

3.5. Stellar Masses

In this section, we describe the methodology and present estimates for the stellar masses of the DOGs in this sample.

3.5.1. Methodology

To estimate stellar masses, we rely on Simple Stellar Population (SSP) template SEDs from the Bruzual & Charlot (2003) population synthesis library. All models used here have ages spaced logarithmically from 10 Myr up to 1 Gyr, solar metallicity, a Chabrier initial mass function (IMF) over the mass range 0.1–100 $M_\odot$ (Chabrier 2003), and use the Padova 1994 evolutionary tracks (Girardi et al. 1996). The reddening law from Calzetti et al. (2000) is used between 0.12 and 2.2 μm and that of Draine (2003) for longer wavelengths. This method is similar to that used in Bussmann et al. (2009).

For sources at $z \sim 2$ whose mid-IR luminosity is dominated by stellar light, IRAC photometry samples the SED over the wavelength range where emission from asymptotic and red giant branch stars as well as low-mass main-sequence stars produces an emission peak at rest frame 1.6 μm. In such cases, for given assumptions regarding the star formation history, metallicity, and IMF, stellar mass estimates can be obtained via stellar population synthesis modeling. One goal of this work is to estimate stellar masses using self-consistent modeling of photometry measured at similar wavelengths for a variety of $z \sim 2$ dusty galaxies. Therefore, we apply this method to determine stellar masses in SMGs as well as XFLS and SWIRE sources. The IRAC data for each of these galaxy populations come from, respectively, Dye et al. (2008), Lacy et al. (2005), and Lonsdale et al. (2009).

The DOGs studied in this paper have mid-IR SEDs that are dominated by a power-law component, suggesting that obscured AGN emission is overwhelming the stellar flux at these wavelengths. The shape of the mid-IR SED therefore provides limited constraints on the stellar population and additional information is needed to estimate the stellar mass of these sources. To overcome this challenge, SSP models were fitted to high spatial-resolution *HST* photometry in the rest-frame UV (WFPC2/F606W or ACS/F814W) and rest-frame optical (NIC2/F160W) from Bussmann et al. (2009). Two sources currently lack *HST* data (SST24 J142827.2+354127 and SST24 J143411.0+331733[9]) and so are excluded from this analysis.

In principle, rest-frame near-IR data offer a means to estimate the SSP age and A_V independently, since rest-frame optical and near-IR photometry sample the SED above the 4000 Å break while the rest-frame UV photometry samples galaxy light below the 4000 Å break. However, these data come from the IRAC 3.6 μm images of the Boötes field (SDWFS; Ashby et al. 2009), where the spatial resolution is insufficient to resolve the nuclear source from the extended galaxy component. In this case, there are only limited constraints on the amount of non-stellar (i.e., obscured AGN) emission at 3.6 μm. We have explored the effect of this uncertainty on the fitting process by artificially reducing the 3.6 μm flux by 50% (corresponding to the situation where the 3.6 μm emission is equal parts starlight and AGN) and re-analyzing the data. Comparing results, we find that higher AGN fractions imply younger inferred SSP ages and higher A_V values. Because the AGN fraction in these sources is currently unknown at 3.6 μm, we are unable to constrain both the age and A_V independently.

[9] *HST* data exist for this source but will be presented in a separate paper (M. Prescott et al. 2010, in preparation).

Although the usage of photometry at different wavelengths is not ideal for the purposes of comparing stellar masses between galaxy populations, this method remains valuable because the models being fitted to the data are the same for each galaxy population. Indeed, recent work has suggested that the dominant source of systematic uncertainty in stellar mass estimates of K-selected galaxies at $z \sim 2.3$ is the use of different stellar population synthesis codes (Muzzin et al. 2009), and that these systematics often dominate the formal random uncertainty. As long as the parameters of the model used here (such as the IMF, star-formation history, metallicity, etc.) do not vary from population to population, the comparison presented here should be valid in a global sense.

3.5.2. Stellar Mass Estimates

Figure 7 shows χ^2_ν contours for a grid of SSP ages and A_V values. The contours trace lines of 80%, 95%, and 99.9% confidence intervals allowed by the photometric uncertainties (estimated using a bootstrap method similar to that outlined in Section 3.3). The solid gray lines trace iso-mass contours and show the range in stellar masses allowed by the photometric uncertainties. The best-fit SSP model parameters ($M_{\rm star}$ and χ^2_ν) are printed in each panel and shown in Table 5.

The stellar masses in the sample range from (1–20) $\times$ 10^{10} $M_\odot$, with a median value of 2×10^{10} $M_\odot$. The χ^2_ν values range from 0.37 to 1.16, with a median value of 0.69. In one case (SST24 J143001.9+334538, or S3), the photometric uncertainty is so large that $\chi^2_\nu < 1$ over the full range of A_V and SSP age that we have sampled and so the range of acceptable fits is very large. For this source, we quote the 3σ upper limit on the stellar mass based on the photometric uncertainty.

The ratio of the stellar to gas mass, $\zeta \equiv M_{\rm star}/M_{\rm gas}$, is a measure of the evolutionary state of the galaxy, with larger values indicating more processing of gas to stars. Our estimates of ζ, computed assuming $M_{\rm gas}/M_{\rm dust} = 120$, are presented in Table 5. We caution that the gas mass to dust mass ratio is highly uncertain. In SMGs, there is evidence suggesting it is $\approx$60 (Kovács et al. 2006). Adopting this lower value would imply lower gas masses by a factor of 2 and hence double our $M_{\rm star}/M_{\rm gas}$ estimates.

Clustering studies suggest that the most luminous DOGs reside in very massive halos ($M_{\rm DM} \sim 10^{13}$ $M_\odot$ Brodwin et al. 2008). It is tempting to attribute the low stellar masses we estimate for DOGs to youth. However, the absolute stellar masses we compute are extremely uncertain. For example, the use of a Salpeter IMF rather than a Chabrier IMF would approximately double our stellar mass estimates (Bruzual & Charlot 2003). Beyond the choice of what IMF slope to use, the mass-to-light ratio of a model galaxy (for a given rest-frame near-UV$-R$ color) can vary significantly depending on the details of its star formation history, the clumpiness of its interstellar medium and the associated dust attenuation law, as well as how advanced stages of stellar evolution are treated, such as blue stragglers, thermally pulsating asymptotic giant branch stars, etc. (Conroy et al. 2009). In light of these uncertainties, the fact that our stellar mass estimates are low ($M_{\rm star} \sim 10^{10}$ $M_\odot$) compared to the dark matter halos in which we believe they reside is not yet a cause for concern—a quantitative study of the maximum possible stellar mass allowed by the photometry (by examining results from different stellar population synthesis codes, star formation histories, metallicities, etc.) would be the best way to approach this issue in the near term, but is beyond the scope of the current work.

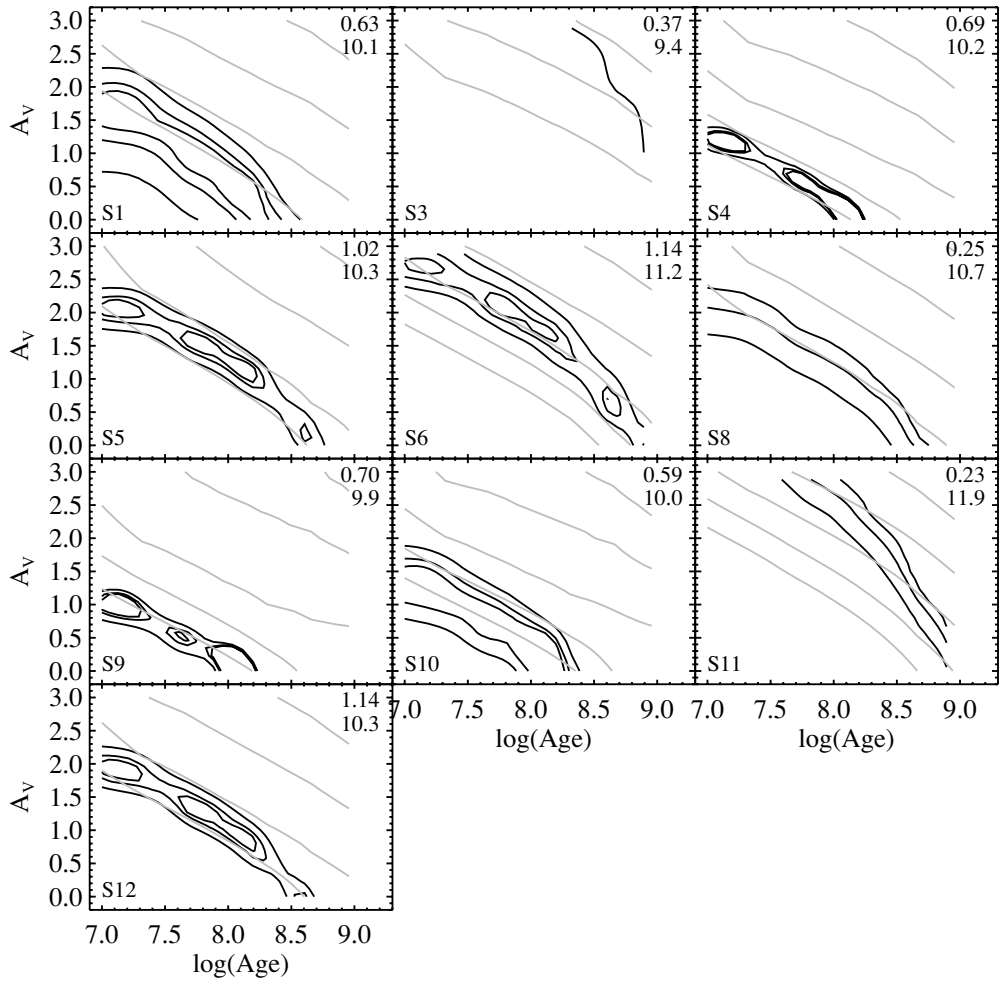

Figure 7. χ^2_ν contours based on SSP fits to *HST* imaging in *H* band and *V*- or *I* band. Black lines indicate 80%, 95%, and 99.9% confidence intervals. Gray contours trace lines of constant stellar mass for the given *HST* photometry, starting with $M_{\rm star} = 10^{10}\ M_\odot$ in the bottom left and increasing by 0.5 dex toward the upper right. In the top right corner of each panel is the minimum χ^2_ν value and the associated stellar mass, in units of $\log(M_{\rm star}/M_\odot)$. The bottom left corner contains the source identifier. Not shown are sources S2 and S7, since these targets have no *HST* imaging available. The best-fit stellar masses range from 10^{10} to $10^{12}\ M_\odot$.

4. DISCUSSION

In this section, we seek to understand the role of DOGs in galaxy evolution and their relation to other high-z galaxy populations. We begin by motivating a comparison sample of such objects, including SMGs and *Spitzer*-selected ULIRGs from the XFLS and SWIRE survey. We then examine how the measured properties differ from population to population. We end with the implications of these comparisons for models of galaxy evolution.

4.1. Related $z \approx 2$ Galaxy Populations

4.1.1. SMGs

SMGs represent an interesting population of galaxies for comparison with DOGs because they are selected at submillimeter wavelengths where the dominant emission component is cold dust ($T_{\rm dust} \sim 30$ K). In contrast, DOGs are selected predominantly by their brightness at 24 μm and therefore should be dominated by hot dust. Despite this fundamental distinction, these two galaxy populations have similar number densities and redshift distributions (Chapman et al. 2005; Dey et al. 2008; Blain et al. 2004). Recent evidence suggests that 24 μm faint ($F_{24\,\mu{\rm m}} \sim 0.1$–$0.5$ mJy) DOGs have a composite SED whose shape in the far-IR closely mimics that of the average bright ($F_{850} > 5$ mJy) SMG (Pope et al. 2008a). Furthermore, 24 μm faint DOGs and SMGs have similar real space correlation lengths ($r_0 \approx 6 \pm 2\ h^{-1}$ Mpc), yet there is tentative evidence that DOG clustering strength increases with 24 μm flux density ($r_0 \approx 13 \pm 3\ h^{-1}$ Mpc for DOGs with $F_{24\,\mu{\rm m}} > 0.6$ mJy; Brodwin et al. 2008). While these results are suggestive of an association between the two populations, the details of such a connection are not yet clear. In an effort to study this connection via their far-IR properties, we will compare the data presented in this paper with SHARC-II 350 μm and MAMBO 1.2 mm imaging of 25 SMGs from the Submillimeter Common-User Bolometer Array (SCUBA) HAlf Degree Extragalactic Survey (Laurent et al. 2006; Kovács et al. 2006; Coppin et al. 2008; Greve et al. 2004).

4.1.2. XFLS Sources

A set of *Spitzer*-selected galaxies from the 4 deg^2 XFLS shares many properties with the 24 μm bright DOGs (Yan et al. 2007). The specific selection criteria are similar, although not necessarily as extreme in their IR-optical flux density ratios: $F_{24\,\mu{\rm m}} \geqslant 0.9$ mJy, $\nu F_\nu(24\,\mu{\rm m})/\nu F_\nu(8\,\mu{\rm m}) \geqslant 3.16$, and $\nu F_\nu(24\,\mu{\rm m})/\nu F_\nu(0.7\,\mu{\rm m}) \geqslant 10$ (in comparison, DOGs have

Table 6
Average High-z Galaxy Properties

Source	R-[24]	N	L_{IR} (10^{12} $L_\odot$)	L_{FIR} (10^{12} $L_\odot$)	T_{dust} (K)	M_d (10^9 $M_\odot$)	M_{star} (10^{10} $M_\odot$)	M_{star}/M_{gas}[a]
Boötes[b]	> 14	5	23	10	45	0.5	>2	> 0.3
XFLS[c]	ALL	11	7.7	2.7	32	5.0	13	0.48
	> 14	6	8.7	1.1	27	7.3	10	0.21
	< 14	5	6.5	4.6	37	2.3	16	0.58
XFLS PAH[c]	ALL	5	5.7	1.8	31	4.6	22	0.54
	> 14	2	6.3	1.6	29	7.5	23	0.30
	< 14	3	5.4	2.0	32	2.8	22	0.69
XFLS weak-PAH[c]	ALL	6	9.4	3.4	32	5.3	5.0	0.25
	> 14	4	3.5	0.8	26	7.2	3.8	0.17
	< 14	2	14	8.0	45	1.6	7.3	0.40
SWIRE[d]	ALL	19	6.5	3.1	32	6.7	28	0.53
	> 14	16	6.7	3.1	32	6.1	28	0.56
	< 14	3	5.5	2.6	30	9.9	24	0.35
SMG[e]	ALL	18	6.9	3.2	35	1.5	10	0.60
	>14	4	7.8	3.6	28	2.9	6.9	0.28
	< 14	14	6.1	2.9	37	1.1	12	0.71

Notes.
[a] Computed using $M_{gas}/M_{dust} = 120$.
[b] Includes only DOGs detected at 350 μm.
[c] XFLS sources with MAMBO 1.2 mm detections (Sajina et al. 2008).
[d] SWIRE sources with MAMBO 1.2 mm detections (Lonsdale et al. 2009).
[e] From compilation of Coppin et al. (2008).

$\nu F_\nu(24\,\mu\text{m})/\nu F_\nu(0.7\,\mu\text{m}) \geqslant 30$). *Spitzer*/IRS spectroscopy of these objects has revealed strong silicate absorption and in some cases PAH emission features on par with those of SMGs (Sajina et al. 2007). This suggests that the XFLS sources are composite AGN/starburst systems and may represent a transition phase between (un)obscured quasars and SMGs (Sajina et al. 2008). MAMBO 1.2 mm observations of 44 XFLS sources have allowed a detailed study of their far-IR properties and have suggested $\langle L_{IR}\rangle >\sim 7 \times 10^{12}\ L_\odot$ (Sajina et al. 2008).

4.1.3. SWIRE Sources

The last set of comparison galaxies we consider is *Spitzer*-selected sources from the SWIRE survey (Lonsdale et al. 2009). Like DOGs in Boötes and the XFLS sources, they have large IR-optical flux density ratios. However, an additional criterion has been applied to identify sources with significant emission at rest frame 1.6 μm due to evolved stellar populations. For sources at $z = 1.5$–3, this means selecting objects whose mid-IR spectrum peaks at 5.8 μm. Although spectroscopic redshifts are not available for most of this sample, SED fitting has suggested photometric redshifts consistent with $z \sim 2$ and stellar masses of $(0.2–6) \times 10^{11}\ M_\odot$ (Lonsdale et al. 2009). MAMBO 1.2 mm photometry for 61 of these SWIRE sources has indicated far-IR luminosities of 10^{12}–$10^{13.3}\ L_\odot$ (Lonsdale et al. 2009).

4.2. Comparison of Measured Properties

Our results from Section 3 represent our best estimates of L_{IR}, L_{FIR}, T_{dust}, M_{dust}, and M_{star} for the DOGs in the sample. In Table 6, we give the median value of these quantities for DOGs in Boötes (from this paper), SMGs, and XFLS and SWIRE sources. In computing these median values, we do not consider sources at $z < 1$; nor do we consider sources without detections at (sub-)millimeter wavelengths (see discussion on caveats to the analysis at the end of this section). Table 6 also makes a distinction between XFLS sources whose mid-IR spectra are dominated by strong PAH features (XFLS PAH) and those that show weak or absent PAH features (XFLS weak-PAH). Each of these galaxy populations is further subdivided into those that qualify as DOGs ($R - [24] > 14$) and those that do not.

The primary feature of this comparison is that the relative uncertainty in the estimated parameters between galaxy populations has been reduced by computing the respective values self-consistently with the methods outlined in Section 3. The exceptions to this rule are L_{IR} and T_{dust} (note that while the photometry used to determine M_{star} for Boötes DOGs is different than for the other galaxy populations, the methodology used is the same, including the use of the same set of model SSP templates). Our method of computing L_{IR} relies on the assumption that Mrk 231 represents a reasonable approximation of the source SED. For many SMGs as well as XFLS and SWIRE sources, this is an unrealistic assumption. Instead, we estimate L_{IR} from L_{FIR}, assuming (1) $L_{IR} = L_{IR,\,SB} + L_{IR,\,AGN}$; (2) $L_{IR,\,SB} = \alpha L_{FIR}$; (3) $L_{IR,\,AGN} = \epsilon L_{IR}$, where α is a factor ≈ 1.3, depending on T_d and β (Helou et al. 1988) and ϵ is the typical AGN fraction of the galaxy population. For SMGs, we adopt the conservative upper limit from Pope et al. (2008b) of $\epsilon = 0.3$. For SWIRE sources and XFLS PAH sources, this fraction is ≈ 0.3 (Pope et al. 2008b; Lonsdale et al. 2009; Sajina et al. 2008), while for XFLS weak-PAH sources we use 0.7 (Sajina et al. 2008).

The T_{dust} values given in the literature are adopted for each source. It should be noted that T_{dust} for SWIRE sources are uncertain due to the lack of data near the far-IR peak (i.e., observed frame 160 or 350 μm). Lonsdale et al. (2009) analyze the stacked signal at 160 μm from these sources and find that the T_{dust} is higher by as much as 10 K than what is assumed in their Table 6. For a given 1.2 mm flux, increasing T_d by 10 K will increase L_{FIR} by a factor of $\approx$3 and decrease M_{dust} by $\approx$50%.

The key result from Table 6 is that while the DOGs in our sample have lower dust masses than the other galaxy populations

by a factor of ∼3–20, they have higher total IR and far-IR luminosities by factors of ∼2. This distinction is driven by the difference in $T_{\rm dust}$, as DOGs in the sample have higher values by ≈10–20 K compared to the other galaxy populations.

In terms of the stellar and gas mass estimates, the relationship between DOGs in Boötes (i.e., the sample studied in this paper) and the remaining galaxy populations is unclear. Even if a single dust temperature and a single dust to gas mass ratio for each of the sources studied in this paper are adopted, the uncertainties on the stellar mass estimates are large enough to allow greatly varying stellar mass to gas mass ratios. Sources satisfying $R - [24] > 14$ (i.e., DOGs) tend to have higher gas masses compared to $R - [24] < 14$ sources (under the assumption of a constant dust-to-gas mass ratio). This difference is at least in part due to a difference in dust temperatures; within this sample, DOGs have lower dust temperatures than non-DOGs. This is in contrast with the evidence for high dust temperatures in the Boötes DOGs studied in this paper and may be an indication that millimeter-detected DOGs represent a special subset of DOGs that is more representative of the millimeter-selected galaxy population than the DOG population.

An important caveat to this comparison is that we are dealing with small sample sizes due to incomplete coverage at one or more bands from the mid- to the far-IR. For instance, while every DOG has a measured 24 μm flux density, very few have been observed at 350 μm, and only two have been observed at 1 mm. Similarly, few XFLS and SWIRE sources have been detected at 1 mm and even fewer have been observed at 350 μm. Although SMGs are the best-studied class of objects within this set of populations, they too suffer from low-number statistics. Larger sample sizes in the critical 200–500 μm regime will arrive following the analysis of wide-field survey data from the Balloon-borne Large Aperture Submillimeter Telescope (e.g., Pascale et al. 2009) and the *Herschel* Space Observatory.

4.3. Implications for Models of Galaxy Evolution

One of the major open questions in galaxy evolution is the effect that AGNs have on their host galaxies. In the local universe, there is observational evidence that ULIRGs dominated by warm dust serve as a transition phase between cold-dust ULIRGs and optically luminous quasars and that this transition may be driven by a major merger (Sanders et al. 1988a, 1988b). Recent theoretical models of quasar evolution based on numerical simulations of major mergers between gas-rich spirals have suggested that the subsequent growth of a supermassive black hole can regulate star formation via a feedback effect which re-injects energy into the interstellar medium (ISM) and expels the remaining gas that would otherwise form stars (Hopkins et al. 2006).

Although the notion that local ULIRGs are associated with mergers is well accepted (e.g., Sanders & Mirabel 1996), the picture is less clear at high redshift. Morphological studies of high-z galaxies suffer from surface brightness dimming, making the detection of faint merger remnant signatures difficult (e.g., Dasyra et al. 2008; Melbourne et al. 2008; Bussmann et al. 2009; Melbourne et al. 2009). However recent theoretical work on the cosmological role of mergers in the formation of quasars and spheroid galaxies suggests that they dominate the $z \gtrsim 1$ quasar luminosity density compared to secular processes such as bars or disk instabilities (Hopkins et al. 2008).

If major mergers drive the formation of massive galaxies at high redshift, then one possible interpretation of our results involves an evolutionary scenario in which these sources represent a very brief but luminous episode of extreme AGN growth just prior to the quenching of star formation. In such a scenario, SMGs and the brightest 24 μm selected sources represent the beginning and end stages, respectively, of the high star formation rate, high IR luminosity phase in massive galaxy evolution. Consistent with this scenario is that we find 24 μm bright DOGs in Boötes to have higher dust temperatures (possibly from AGN heating of the dust) than SMGs and less extreme *Spitzer*-selected sources. We caution, however, that these results are consistent with any evolutionary model in which the 24 μm bright phase follows the submillimeter bright phase, be it driven by major mergers, minor mergers, or some secular process.

Finally, we stress that larger samples of millimeter and submillimeter imaging of *Spitzer*-selected galaxies are needed in order to understand their role in galaxy evolution fully by comparing samples of similar number density, clustering properties, etc. Much of this will be provided by upcoming *Herschel* and SCUBA-2 surveys. In the more immediate future, 1 mm imaging with currently available instruments such as the Astronomical Thermal Emission Camera (AzTEC) and the MAx-Planck Millimeter BOlometer Array (MAMBO) will be critical to constraining the cold-dust properties of *Spitzer*-selected galaxies. Only when these surveys have obtained statistically significant numbers of detections or stringent upper limits will we be able to make definitive conclusions regarding the nature of the link between AGNs and starbursts in the formation of the most massive galaxies.

5. CONCLUSIONS

We present CSO/SHARC-II 350 μm and CARMA 1 mm photometry of DOGs in the Boötes Field. The major results and conclusions from this study are the following:

1. At 350 μm, 4/5 DOGs are detected in data with low rms levels ($\leqslant$ 15 mJy) and 0/8 DOGs are detected in data with medium to high rms levels (20–50 mJy). At 1 mm, a subset of two DOGs was observed but not detected.
2. Mrk 231 is confirmed as a valid template for the SEDs of the DOGs in this sample. This suggests that the 24 μm bright ($F_{24\,\mu{\rm m}} \gtrsim 1$ mJy) population of DOGs is dominated by the warm dust, possibly heated by an AGN. Cold dust templates such as Arp 220 are inconsistent with the data in all 12 objects studied.
3. Trends in the flux density ratios 350 μm/24 μm and 1200 μm/24 μm with the $R - [24]$ color ($F_{24\,\mu{\rm m}}/F_{0.7\,\mu{\rm m}}$) show that DOGs in this sample have elevated 24 μm emission relative to SMGs, most likely due to an obscured AGN.
4. The non-detections at 1 mm imply $T_{\rm dust}$ greater than 35–60 K for two objects.
5. If the dust properties of the two DOGs observed at 1 mm apply generally to the 24 μm bright DOGs, then we estimate dust masses for these sources of $1.6–6.1 \times 10^8\ M_\odot$. Lower $T_{\rm dust}$ would imply higher dust masses and vice versa.
6. In comparison to other $z \approx 2$ ULIRGs, DOGs have warmer dust temperatures that imply higher IR luminosities and lower dust masses. This may be an indication that AGN growth has heated the ambient ISM in these sources.
7. Our stellar mass estimates provide weak evidence indicating that the 24 μm bright DOGs may have converted more gas into stars than SMGs or other *Spitzer*-selected sources, consistent with them representing a subsequent phase of evolution. An important caveat to this conclusion is that we have assumed that DOGs and SMGs share the same

gas mass to dust mass ratio. Testing this assumption will require new data and will be an important goal of future work.

This work is based in part on observations made with the *Spitzer Space Telescope*, which is operated by the Jet Propulsion Laboratory, California Institute of Technology under NASA contract 1407. *Spitzer*/MIPS guaranteed time observing was used to image the Boötes field at 24 μm and is critical for the selection of DOGs. We thank the SDWFS team (particularly Daniel Stern and Matt Ashby) for making the IRAC source catalogs publicly available. Data from the original IRAC shallow survey were used for initial stellar mass estimates. We thank the anonymous referee for a thorough review of the manuscript that helped improve the paper.

We are grateful to the expert assistance of the staff of Kitt Peak National Observatory where the Boötes field observations of the NDWFS were obtained. The authors thank NOAO for supporting the NOAO Deep Wide-Field Survey. In particular, we thank Jenna Claver, Lindsey Davis, Alyson Ford, Emma Hogan, Tod Lauer, Lissa Miller, Erin Ryan, Glenn Tiede and Frank Valdes for their able assistance with the NDWFS data. We also thank the staff of the W. M. Keck Observatory, where some of the galaxy redshifts were obtained.

R.S.B. gratefully acknowledges financial assistance from *HST* grant GO10890, without which this research would not have been possible. Support for Program number HST-GO10890 was provided by NASA through a grant from the Space Telescope Science Institute, which is operated by the Association of Universities for Research in Astronomy, Incorporated, under NASA contract NAS5-26555. The research activities of A.D. are supported by NOAO, which is operated by the Association of Universities for Research in Astronomy (AURA) under a cooperative agreement with the National Science Foundation. Support for E. Le Floc'h was provided by NASA through the *Spitzer Space Telescope* Fellowship Program.

Facilities: Spitzer, CSO, and CARMA. This research made use of CSO (SHARC-II) and CARMA data. Support for CARMA construction was derived from the states of California, Illinois, and Maryland, the Gordon and Betty Moore Foundation, the Kenneth T. and Eileen L. Norris Foundation, the Associates of the California Institute of Technology, and the National Science Foundation. Ongoing CARMA development and operations are supported by the National Science Foundation under a cooperative agreement, and by the CARMA partner universities.

REFERENCES

Ashby, M. L. N., et al. 2009, ApJ, 701, 428
Blain, A. W., Chapman, S. C., Smail, I., & Ivison, R. 2004, ApJ, 611, 725
Brand, K., et al. 2008, ApJ, 680, 119
Brodwin, M., et al. 2008, ApJ, 687, L65
Bruzual, G., & Charlot, S. 2003, MNRAS, 344, 1000
Bussmann, R. S., et al. 2009, ApJ, 693, 750
Calzetti, D., Armus, L., Bohlin, R. C., Kinney, A. L., Koornneef, J., & Storchi-Bergmann, T. 2000, ApJ, 533, 682
Caputi, K. I., et al. 2007, ApJ, 660, 97
Casey, C. M., et al. 2009, MNRAS, arXiv:0906.5346v1
Chabrier, G. 2003, PASP, 115, 763
Chapman, S. C., Blain, A. W., Smail, I., & Ivison, R. J. 2005, ApJ, 622, 772
Conroy, C., Gunn, J. E., & White, M. 2009, ApJ, 699, 486
Coppin, K., Halpern, M., Scott, D., Borys, C., & Chapman, S. 2005, MNRAS, 357, 1022
Coppin, K., et al. 2008, MNRAS, 384, 1597
Dasyra, K. M., Yan, L., Helou, G., Surace, J., Sajina, A., & Colbert, J. 2008, ApJ, 680, 232
de Vries, W. H., Morganti, R., Röttgering, H. J. A., Vermeulen, R., van Breugel, W., Rengelink, R., & Jarvis, M. J. 2002, AJ, 123, 1784
Desai, V., et al. 2006, ApJ, 641, 133
Dey, A., et al. 2005, ApJ, 629, 654
Dey, A., et al. 2008, ApJ, 677, 943
Donley, J. L., Rieke, G. H., Pérez-González, P. G., Rigby, J. R., & Alonso-Herrero, A. 2007, ApJ, 660, 167
Draine, B. T. 2003, ARA&A, 41, 241
Dunne, L., & Eales, S. A. 2001, MNRAS, 327, 697
Dunne, L., Eales, S. A., & Edmunds, M. G. 2003, MNRAS, 341, 589
Dunne, L., Eales, S., Edmunds, M., Ivison, R., Alexander, P., & Clements, D. L. 2000, MNRAS, 315, 115
Dye, S., et al. 2008, MNRAS, 386, 1107
Eisenhardt, P. R., et al. 2004, ApJS, 154, 48
Faber, S. M., et al. 2003, Proc. SPIE, 4841, 1657
Fiore, F., et al. 2008, ApJ, 672, 94
Fiore, F., et al. 2009, ApJ, 693, 447
Franceschini, A., Aussel, H., Cesarsky, C. J., Elbaz, D., & Fadda, D. 2001, A&A, 378, 1
Gallagher, S. C., Brandt, W. N., Chartas, G., Garmire, G. P., & Sambruna, R. M. 2002, ApJ, 569, 655
Girardi, L., Bressan, A., Chiosi, C., Bertelli, G., & Nasi, E. 1996, A&AS, 117, 113
Greve, T. R., Ivison, R. J., Bertoldi, F., Stevens, J. A., Dunlop, J. S., Lutz, D., & Carilli, C. L. 2004, MNRAS, 354, 779
Helou, G., Khan, I. R., Malek, L., & Boehmer, L. 1988, ApJS, 68, 151
Hildebrand, R. H. 1983, QJRAS, 24, 267
Hopkins, P. F., Hernquist, L., Cox, T. J., Di Matteo, T., Robertson, B., & Springel, V. 2006, ApJS, 163, 1
Hopkins, P. F., Hernquist, L., Cox, T. J., & Kereš, D. 2008, ApJS, 175, 356
Houck, J. R., et al. 2004, ApJS, 154, 18
Houck, J. R., et al. 2005, ApJ, 622, L105
Hughes, D. H., Dunlop, J. S., & Rawlings, S. 1997, MNRAS, 289, 766
Hughes, D. H., Gear, W. K., & Robson, E. I. 1994, MNRAS, 270, 641
Hutchings, J. B., & Neff, S. G. 1987, AJ, 93, 14
Kovács, A. 2006, PhD thesis, Caltech
Kovács, A., Chapman, S. C., Dowell, C. D., Blain, A. W., Ivison, R. J., Smail, I., & Phillips, T. G. 2006, ApJ, 650, 592
Lacy, M., et al. 2005, ApJS, 161, 41
Laurent, G. T., et al. 2006, ApJ, 643, 38
Le Floc'h, E., et al. 2005, ApJ, 632, 169
Leong, M., Peng, R., Houde, M., Yoshida, H., Chamberlin, R., & Phillips, T. G. 2006, Proc. SPIE, 6275, 21
Lonsdale, C. J., et al. 2009, ApJ, 692, 422
Melbourne, J., et al. 2008, AJ, 136, 1110
Melbourne, J., et al. 2009, AJ, 137, 4854
Muzzin, A., Marchesini, D., van Dokkum, P. G., Labbé, I., Kriek, M., & Franx, M. 2009, ApJ, 701, 183
Oke, J. B., et al. 1995, PASP, 107, 375
Papovich, C., et al. 2007, ApJ, 668, 45
Pascale, E., et al. 2009, arXiv:0904.1206P
Pérez-González, P. G., et al. 2005, ApJ, 630, 82
Polletta, M., Weedman, D., Hönig, S., Lonsdale, C. J., Smith, H. E., & Houck, J. 2008, ApJ, 675, 960
Pope, A., et al. 2008a, ApJ, 689, 127
Pope, A., et al. 2008b, ApJ, 675, 1171
Rieke, G. H., Alonso-Herrero, A., Weiner, B. J., Pérez-González, P. G., Blaylock, M., Donley, J. L., & Marcillac, D. 2009, ApJ, 692, 556
Rieke, G. H., & Lebofsky, M. J. 1981, ApJ, 250, 87
Rieke, G. H., et al. 2004, ApJS, 154, 25
Rigopoulou, D., Lawrence, A., & Rowan-Robinson, M. 1996, MNRAS, 278, 1049
Sajina, A., Yan, L., Lacy, M., & Huynh, M. 2007, ApJ, 667, L17
Sajina, A., et al. 2008, ApJ, 683, 659
Sanders, D. B., Mazzarella, J. M., Kim, D.-C., Surace, J. A., & Soifer, B. T. 2003, AJ, 126, 1607
Sanders, D. B., & Mirabel, I. F. 1996, ARA&A, 34, 749
Sanders, D. B., Soifer, B. T., Elias, J. H., Madore, B. F., Matthews, K., Neugebauer, G., & Scoville, N. Z. 1988a, ApJ, 325, 74
Sanders, D. B., Soifer, B. T., Elias, J. H., Neugebauer, G., & Matthews, K. 1988b, ApJ, 328, L35
Sault, R. J., Teuben, P. J., & Wright, M. C. H. 1995, in ASP Conf. Ser. 77, Astronomical Data Analysis Software and Systems IV, ed. R. A. Shaw, H. E. Payne, & J. J. E. Hayes (San Francisco, CA: ASP), 433

Silva, L., Granato, G. L., Bressan, A., & Danese, L. 1998, ApJ, 509, 103
Soifer, B. T., Sanders, D. B., Neugebauer, G., Danielson, G. E., Lonsdale, C. J., Madore, B. F., & Persson, S. E. 1986, ApJ, 303, L41
Tyler, K. D., et al. 2009, ApJ, 691, 1846
Wang, R., et al. 2008, ApJ, 687, 848
Weedman, D., et al. 2006a, ApJ, 653, 101
Weedman, D. W., et al. 2006b, ApJ, 651, 101
Wilson, C. D., et al. 2008, ApJS, 178, 189
Yan, L., et al. 2004, ApJS, 154, 60
Yan, L., et al. 2007, ApJ, 658, 778
Yang, M., & Phillips, T. 2007, ApJ, 662, 284
Younger, J. D., et al. 2009, MNRAS, 394, 1685